Astron. Astrophys. 240, 385–399 (1990)

ASTRONOMY
AND
ASTROPHYSICS

IRAS observations of RCW 86

H. Greidanus[1] **and R. G. Strom**[2]

[1] Sterrewacht Leiden, Postbus 9513, NL-2300 RA Leiden, The Netherlands
[2] Netherlands Foundation for Research in Astronomy, Postbus 2, NL-7990 AA Dwingeloo, The Netherlands

Received February 22, accepted June 4, 1990

Abstract. Infrared maps and fluxes of the historical supernova remnant RCW 86 (MSH 14-6*3*) are obtained from the IRAS data base. Great care is taken to isolate the remnant's weak emission from the confusing background, which includes the carbon star CS 2178. It is found that the infrared brightness distribution, which is dominated by a concentration in the southwest, correlates well with X-ray, optical and radio images. The spectrum can be modelled by shock-heated dust, radiating at a temperature of 65 ± 3 K with a 60 μm flux density of 64 ± 7 Jy, whence a radiating dust mass of $0.6 \pm 0.1 \; 10^{-3} \, M_\odot$ is derived. A careful comparison of the infrared with previous X-ray results indicates a deficiency of dust by a factor of ~10 with respect to standard values. Based on the dust and coronal gas temperatures, and independently from the absolute flux densities, a density of the surrounding medium of $0.6 \pm 0.1 \, \mathrm{cm}^{-3}$ is derived, compared to $1.1 \pm 0.3 \, \mathrm{cm}^{-3}$ as previously found from X-ray data in the southwestern part of the remnant. The parameters of RCW 86 are compared with those of the three other historical remnants Tycho, Kepler and Cas A. In this series, the infrared temperature is found to decrease with age; for all four remnants the infrared and X-ray derived densities are comparable, while the X-ray masses are an order of magnitude larger than the infrared masses.

Key words: supernova remnants: RCW 86 – infrared radiation – interstellar medium: dust – shock waves

1. Introduction

The supernova remnant RCW 86, also designated G 315.4-2.3 or MSH 14-6*3*, is probably associated with the guest star observed by the Chinese in A. D. 185 (Clark & Stephenson 1977), although this identification is by no means undisputed (e. g. Huang & Moriarty-Schieven 1987). It is a shell-type SNR as demonstrated by its radio image (Caswell et al. 1975), with a radius of ~20′. In the optical there are two different sets of filaments associated with the shell, one in the north and one in the southwest; the latter have been studied spectroscopically by Ruiz (1981), Leibowitz & Danziger (1983) and in the near-infrared by Dennefeld (1986). From the line ratios, shock velocities of $\sim 100 \, \mathrm{km \, s^{-1}}$ and pre-shock densities of $\sim 100 \, \mathrm{cm}^{-3}$ are deduced. A hotter component was observed by Lucke et al. (1979) in coronal [Fe XIV] at a CIE temperature (assuming Collisional Ionization Equilibrium) of $\sim 0.2 \; 10^7$ K. X-ray spectra have been published by Naranen et al. (1977), Winkler (1978), Nugent et al. (1984) and Claas et al. (1989), and X-ray images have been published by the latter authors and by Pisarki et al. (1984). The spectra have been fitted by two-temperature CIE models, with the low temperature component at 0.25–0.6 10^7 K and the high one at 3.9 to >6 10^7 K. In these models, the hot component has been ascribed to the SN blast wave through the interstellar medium, and the cool component to the reverse shock in the ejecta. However, with NEI models (assuming Non-Equilibrium Ionization) the need for the cool component is eliminated.

A number of authors have discussed the distance to RCW 86 in terms of the Σ-D relation and derive values of 2.0–3.2 kpc (Milne 1970; Ilovaisky & Lequeux 1972; Clark & Caswell 1976); the Σ-D relation has been widely challenged however (e. g. Green 1984), and in any case needs a more subtle application (Berkhuijsen 1986; Huang & Thaddeus 1985). If the remnant is associated with a nearby OB association, its distance must be 2.5 kpc (Westerlund 1969). The optical extinctions imply distances of 1 (Ruiz 1981) to 3.2 kpc (Leibowitz & Danziger 1983); the extinction varies however by a factor of 2 (even up to 10 in one location) over the remnant. On the assumption that the remnant is in the Sedov phase and its age is 1800 yr, the X-ray data imply distances of 0.7 (Pisarski et al. 1984, CIE; Nugent et al. 1984, NEI, age is derived) and 1.1 kpc (Claas et al. 1989, NEI); also on this assumption, a type I SN event is indicated. Based upon the alternative assumption, that the remnant is freely expanding, Pisarski et al. find that their data are marginally consistent with a Type II event (but in that case exclude Type I).

Although the historical information on SN 185 is too scanty to decide with any degree of certainty what its type was, several pieces of indirect evidence lead us to favor a Type I event. In the first place, X-ray spectral data (Pisarski et al. 1984; Claas et al. 1989) provide estimates of the hydrogen column density along the line of sight consistent with a distance near 1 kpc, which would preclude the progenitor's membership of the OB association. Secondly, Pisarski et al. use their imaging data to essentially exclude the presence of a neutron star in RCW 86. Both of these facts argue against the progenitor having been a massive star, and are hence inconsistent with a Type II event. Furthermore, at a distance of 1 kpc (corrected for extinction) the object observed in A.D. 185 has an estimated peak absolute visual magnitude of $M_v \simeq -19$ (Pisarski et al. 1984), consistent with a Type I supernova. At twice the distance, this would become $\simeq -21$, too bright for either a Type I or the less luminous Type II event. Finally, we note that the brighter optical emission from RCW 86 is

---

Send offprint requests to: R. G. Strom both kinematically (velocities of several hundreds of km s^{-1}) and physically (apart from a possible Fe deficiency) similar to Kepler (Leibowitz & Danziger, 1983), while both are quite different from the filaments seen in Cas A which is generally believed to have had a massive progenitor. Moreover, the fainter emission along the northern rim is probably shocked interstellar hydrogen, as found in the other young remnants of Type II supernovae, Kepler, Tycho and SN 1006. Consequently, we will assume that RCW 86 resulted from a Type I supernova, and adopt a distance of 1 kpc.

Recently, some IRAS results on RCW 86 have been published by Dwek et al. (1987b) and Dwek (1988). These authors find a correlation between the infrared and X-ray maps, and a strong infrared excess with respect to their emission model.

2. Observations

The Infrared Astronomical Satellite IRAS surveyed almost the entire sky at infrared wavelengths during its mission in 1983 (Neugebauer et al. 1984). The characteristics of the satellite and its observing program have been comprehensively described by Beichmann et al. (1988). No "AO's" (additional, pointed observations) were made for RCW 86, but the object was covered by the survey operations, which were sensitive in four broad wavelength bands centered at 12, 25, 60, and 100 μm, referred to as bands 1 through 4. We have used the Skyflux product, in which the survey scans have been brought to a common resolution and gridded onto 16°-sized maps, and we have co-added original survey scans to make maps of RCW 86 and determine its flux densities.

2.1. Survey scans co-add

All survey scans that passed within 0°75 of the center of RCW 86 ($\alpha, \delta = 219°750$, $-62°283$) have been selected from the IRAS survey data base. (All coordinates are quoted for equinox 1950.) They total 23 in number, although one of the scans was not available to us and could not be used. This is not of great consequence, however, as the coverage is complete even without that scan and the data are not noise limited. A map was made by co-adding (re-gridding) sections of all these scans of size 1°5 × 0°5 (in-scan × cross-scan). In this process the baselines of all individual scans were removed. The resulting map is shown in Fig. 1.

The survey instrument used rectangular detectors, with the short dimension parallel to the scan direction. This produces a rectangularly shaped detector beam (instrumental point spread function), with a nominal resolution of 6′9 (cross-scan) for all four wavelength bands, and 1′1, 1′1, 2′1, 4′3 (in-scan) at 12, 25, 60, 100 μm respectively. As there are a number of such detectors in the focal plane, in addition to a few "edge detectors" having a smaller field of view, and as the scans were oriented at various position angles, the resulting beam on the combined image deviates from this rectangular shape, varying somewhat across the map. By measuring 9 point sources in the map, at 12 μm an average beamsize of 3′6 × 1′0 FWHM is obtained, with the same beamsize indicated for 25 μm. At the longer wavelengths, however, point sources disappear, but beamsizes of 5′2 × 2′1 and 6′4 × 4′3 are estimated for 60 and 100 μm respectively.

Although these maps are at the highest resolution attainable with IRAS (excluding AO's), the background confusion presents severe problems with regard to their analysis. A spectral decomposition technique, separating source and background on the basis of their spectral difference, provides a means of tackling these problems. For this technique the four bands must be mapped at the same resolution, however, hence the Skyflux maps are most suitable for any further reduction.

2.2. Skyflux maps

The IRAS Skyflux product combines all survey scans that have been "hours-confirmed" into three independent data bases, each consisting of maps at the four bands, brought to the same resolution of ~5′; here too, the beam varies slightly with position. RCW 86 was covered by all three "HCON's"; the HCON-1 maps after destriping (see below) are plotted in Fig. 3.

The main emission components contributing to the IRAS maps are: (1) stars, appearing as point sources at 12 (and 25) μm; (2) zodiacal emission, causing a smooth component that dominates at 25 μm, also strong at 12 and 60 μm; (3) cold, galactic dust dominating at 100 μm. The galactic dust emission is mainly concentrated at the galactic plane, while the zodiacal emission is strongest in the ecliptic plane, but still prominent at the ecliptic poles. The only contribution that is expected to vary between the three HCON's is the zodiacal one, as that is the result of the line-of-sight integration through the zodiacal dust cloud within the solar system, which can be along different paths depending on the satellite orbital position and orientation.

2.2.1. Destriping

The striping visible in the raw Skyflux maps of Fig. 2 is due to baseline errors and varying contributions of zodiacal emission in the different scans. In a first analysis, the brightness distribution of RCW 86 was found to be severely influenced by this striping, and therefore an attempt was made to remove this effect. An algorithm was developed to perform an *ad hoc* removal of the stripes based on their additive nature and on the fact that the striping is in the scan direction, which is fixed and known for each HCON. The following process was used. First, the maps were rotated so that the scan direction was parallel to one of the sampling axes; the pixels in this rotated map will be refered to by M_{ij}, with i the axis parallel to the scan direction. Then, the median value of the pixels along axis i was calculated for each j:

$$B_j = \frac{1}{n} \sum_{i=1}^{n} M_{ij} .$$

B_j thus contains the average background as a function of the cross-scan coordinate, and the smallest spatial component present in B_j represents most of the striping. The striping component can then by isolated by applying a high-pass filter to B_j, yielding $\tilde{B}_j$, and can subsequently be subtracted from the rotated map: $\tilde{M}_{ij} = M_{ij} - \tilde{B}_j$. The exact cutoff for the high-pass filter depends on the amount of large-scale spatial information that one wants to retain. For the present purpose, which is isolation of RCW 86, we want in fact to remove all large-scale brightness variations as these are only the background contributions of zodiacal and galactic dust. Finally, the maps are rotated back to their original orientation.

For this technique to work properly, several conditions must be satisfied. In order that real cross-scan brightness variations in the object of interest are not removed together with the stripes, the field to be destriped must be extended enough in the scan direction; using a median instead of a mean in the calculation of B_j then excludes contributions of the object. To still find the stripes on the other hand, the background should be reasonably well described by the in-scan averaged B_j; this is equivalent to the condition that the field must not be too large. For RCW 86 and its

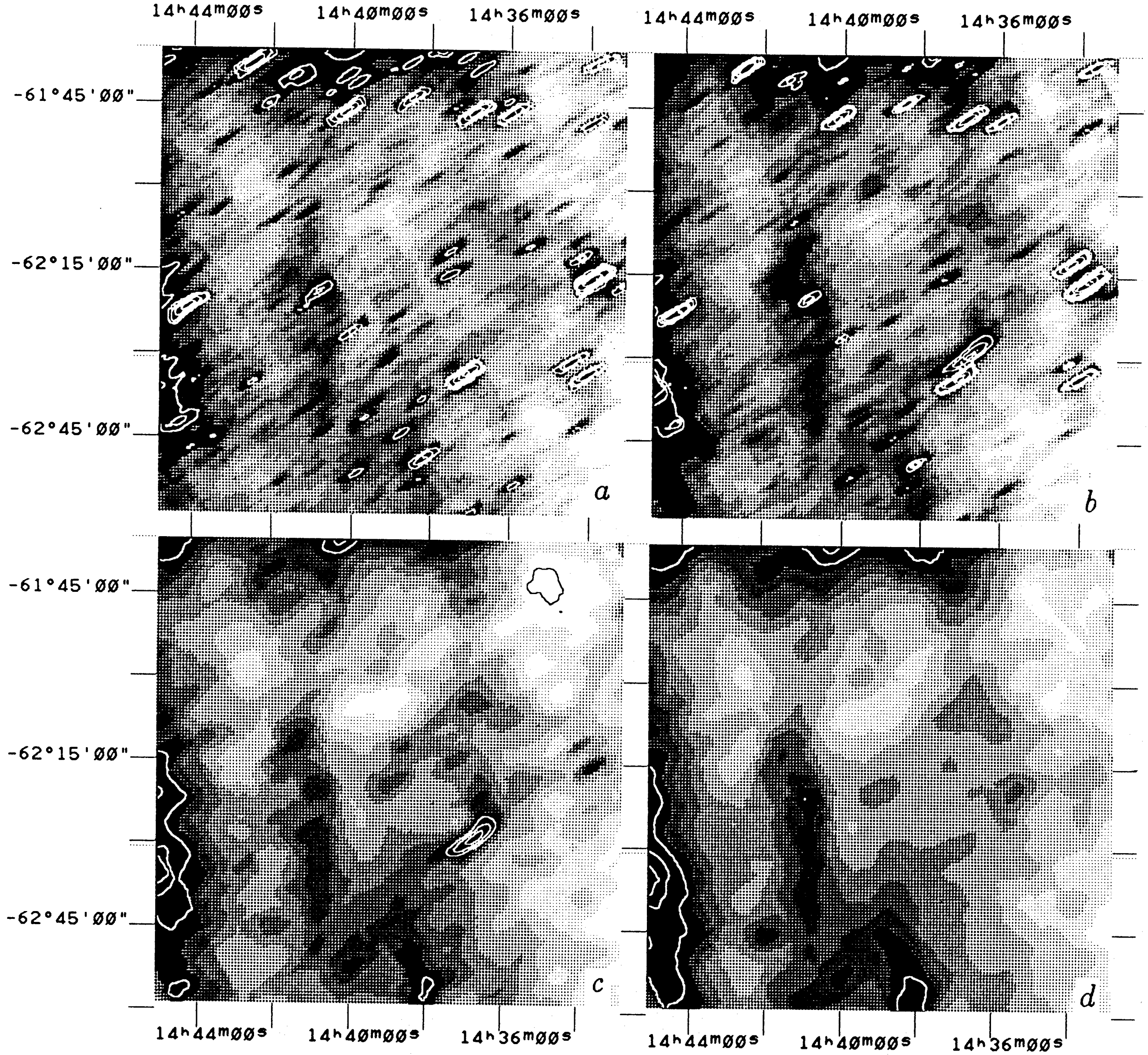

Fig. 1a–d. Maps of RCW 86 at (**a–d**) 12, 25, 60 and 100 μm from co-added IRAS survey scans. The grey scale is linear

surroundings, a field of ~3° satisfies these criteria. Furthermore, only constant, additive baseline offsets are removed in this way. Sloping baselines are not removed and in fact, striping that still remains after this procedure is mainly due to that effect.

This destriping process was applied to 3.°2-sized Skyflux maps, and the effect in bands 1 and 2 of HCON-1 can be judged from comparing Figs. 2 and 3; the other two HCON's and bands are similarly improved. In these images, $\tilde{B}_j$ was obtained by fitting a third degree polynomial to B_j, effectively removing all stripes but retaining the large-scale structure for comparison with the original maps.

2.2.2. Spectral decomposition

As noted above, the dominant emission at 25 μm is from zodiacal dust and at 100 (and 60) μm from galactic dust. After destriping, the zodiacal emission has no small-scale spatial structure, only rising smoothly towards the ecliptic. As RCW 86 is at ecliptic latitude $\beta = -43.°9$, the zodiacal emission distribution in the 3.°2 field is very well approximated by a plane; it may simply be removed by a suitable fitting routine. The galactic dust emission however shows structural variations with large amplitudes on all scales. It can therefore not be very well isolated or subtracted, and in particular assuming a constant background over the area of the object of interest (~0.°5 for RCW 86) can introduce large errors (depending on the relative brightness of the object). As RCW 86 is so weak that it can hardly even be recognized on the raw maps, a different approach is necessary. We have used the spectral decomposition technique developed by Braun (Braun 1985; Braun et al. 1986). Instead of assuming a constant value (or any other simple form such as a plane) for the background to be subtracted, this method assumes that the spectra of object and background do

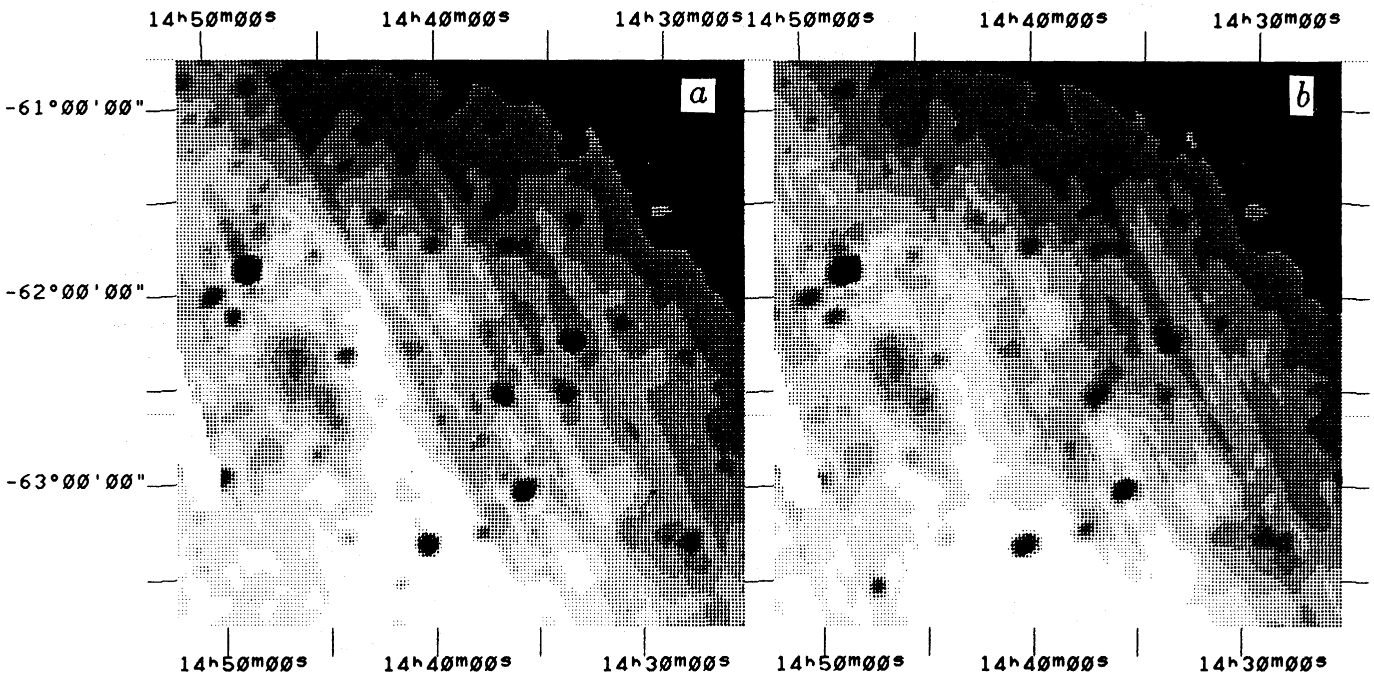

Fig. 2a and b. Skyflux HCON-1 maps in bands 1 (**a**) and 2 (**b**) of the 3° region around RCW 86. The grey scale is based on a histogram of the intensities

not vary spatially. Given an initial estimate of the normalized spectra of object and background, the intensities of these two components may be calculated, independently at each point in the map, from a least-squares fit to the measured intensities in the four wavelength bands. In fact, with four bands, three components may be fitted by least-squares, each with a given (normalized) spectrum. As the spectra are not known a priori, an iterative procedure is necessary. The deviations of the real spectrum of a component from its assumed value can be estimated by examining the derived spatial distributions of the three components, together with the formal fitting error. A correlation or anti-correlation in the spatial distributions of the components indicates that the fitting has tried to mimic the real spectrum of a component present in the map by a linear combination of the assumed component spectra. If, after a number of iterations, a situation is achieved in which (1) the spatial distribution of the three components shows no (anti-)correlation, (2) all components are positive, and (3) the formal fitting errors are acceptable, then the decomposition has succeeded and the spectra and morphologies of the three components are known.

The necessary condition for this technique, that the emission can be described by three components with a spatially constant spectrum, only needs to hold for the area of interest; also, when for example no stellar component is used in the fit, the procedure breaks down at the locations of stars, but that does not affect neighbouring points. When the condition of constant spectrum is unfulfilled, it becomes evident from the fact that no spectra satisfying the three aforementioned criteria can be found. The technique is most reliable when the three components are spectrally very different; should the three spectra not be linearly independent, there is of course no unique solution. In the same way, when two components are morphologically similar, it becomes very difficult to separate them. The result of the spectral decomposition is greatly improved by the destriping procedure, as the spectral variations accompanying the striping would otherwise produce a deterioration of the result.

Table 1. Spectrum and intensity of zodiacal and cold galactic dust emission near RCW 86; the intensity is in MJy/sr, in band 2 for the zodiacal emission and in band 4 for the galactic dust

Band	Zodiacal dust			Cold galactic dust
	HCON-1	HCON-2	HCON-3	
1	0.483	0.496	0.566	0.040±0.01
2	1	1	1	0.040±0.01
3	0.240	0.229	0.249	0.195±0.01
4	0.133	0.121	0.132	1
Intensity	36.19	29.70	40.88	90–240

The spectral decomposition was applied to the destriped Skyflux maps. The fitted components were: zodiacal emission (maximum in band 2), the emission from RCW 86 (maximum in band 3) and galactic cold dust emission (maximum in band 4). The derived flux contributions by the zodiacal emission are somewhat different for each HCON, as expected, and are listed in Table 1. These values were subtracted as constants from the maps, as the large gradient of the galactic emission obscured the gradient in the zodiacal emission towards the ecliptic. Because the galactic emission is so strong especially in band 4, the amount of zodiacal emission present in that band is very difficult to estimate; in particular, it is impossible to decide whether any constant offset (structureless component) is due to galactic or zodiacal dust. This has consequences for the derived flux ratios of these two components, but not for RCW 86, as the two components are ultimately subtracted off.

The flux ratios for the zodiacal component cannot be fit by a single temperature black body spectrum, even when band 4 is not taken into account. This is not surprising as the zodiacal dust encountered along the line of sight must have a large temperature

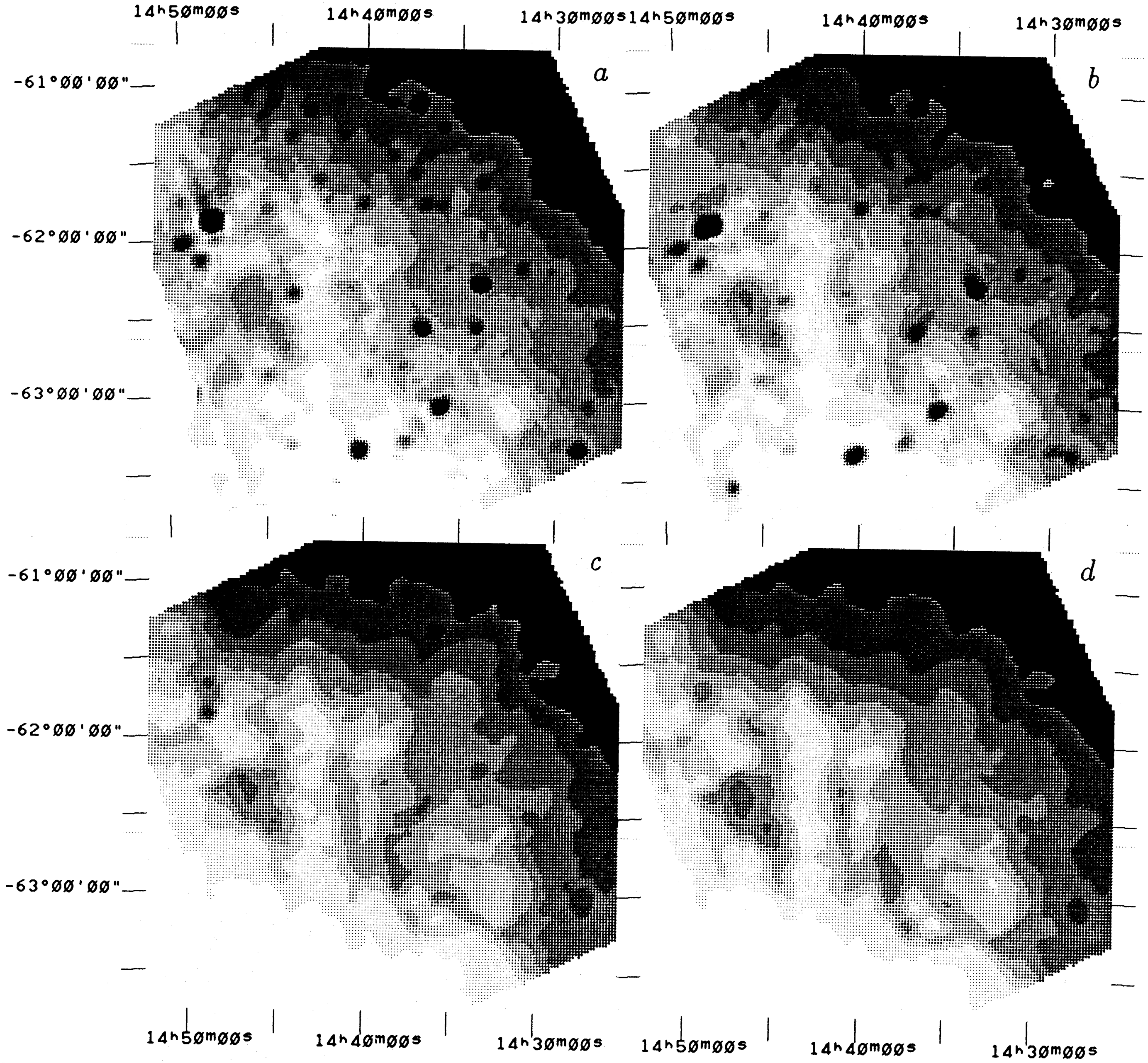

Fig. 3a–d. Destriped Skyflux HCON-1 maps in (a–d) bands 1–4 of the 3° region around RCW 86. The grey scale is based on a histogram of the intensities

gradient in the solar radiation field. A fit of a Planck spectrum convolved with the IRAS spectral responsivities to the flux ratios gives $T_{1/2}=245\pm10$ K (from the band 1/band 2 ratio), and $T_{3/2}=381\pm10$ K. On the other hand, when the black body spectrum is modified by taking into account an absorption efficiency of the dust grains of the from $Q_\lambda \propto \lambda^n$, $n\sim -1\cdots -2$, the fluxes in bands 1 to 3 may be fitted by a single temperature; with $n=-1.5$, $T=172\pm5$ K.

Comparing these values with Deul & Wolstencroft (1988), the flux ratios that appear in the example of their Fig. 5 are ≈ 0.49 for band 1, 0.26–0.36 for band 3 and 0.16–0.25 for band 4. The flux in band 2 at ecliptic latitude $\beta=-43°$ is 35 ± 5 MJy/sr. Considering the uncertainties in band 4, these values are consistent with ours. They are able to fit the zodiacal emission with a one-temperature Planck model, but that is at the ecliptic pole, where they argue that the main contribution is from dust at 1 AU from the sun, hence at constant temperature.

The derived spectrum for the cold galactic dust is also listed in Table 1. (All errors quoted are 1σ values.) This is actually the spectrum characterizing the fraction of the galactic dust that shows spatial structure within the field; any spatially flat fraction (with a different spectrum) cannot be separated from the zodiacal emission. The map of this dust component is shown in Fig. 4. The spectrum cannot be fitted by a single temperature for any value of n in the $\propto\lambda^n$ dust opacity: there always remains an excess at 25 and 12 µm. Temperatures and column densities derived from the 60/100 µm ratio assuming various dust opacity laws are summarized in Table 2. They are normalized to the dust model

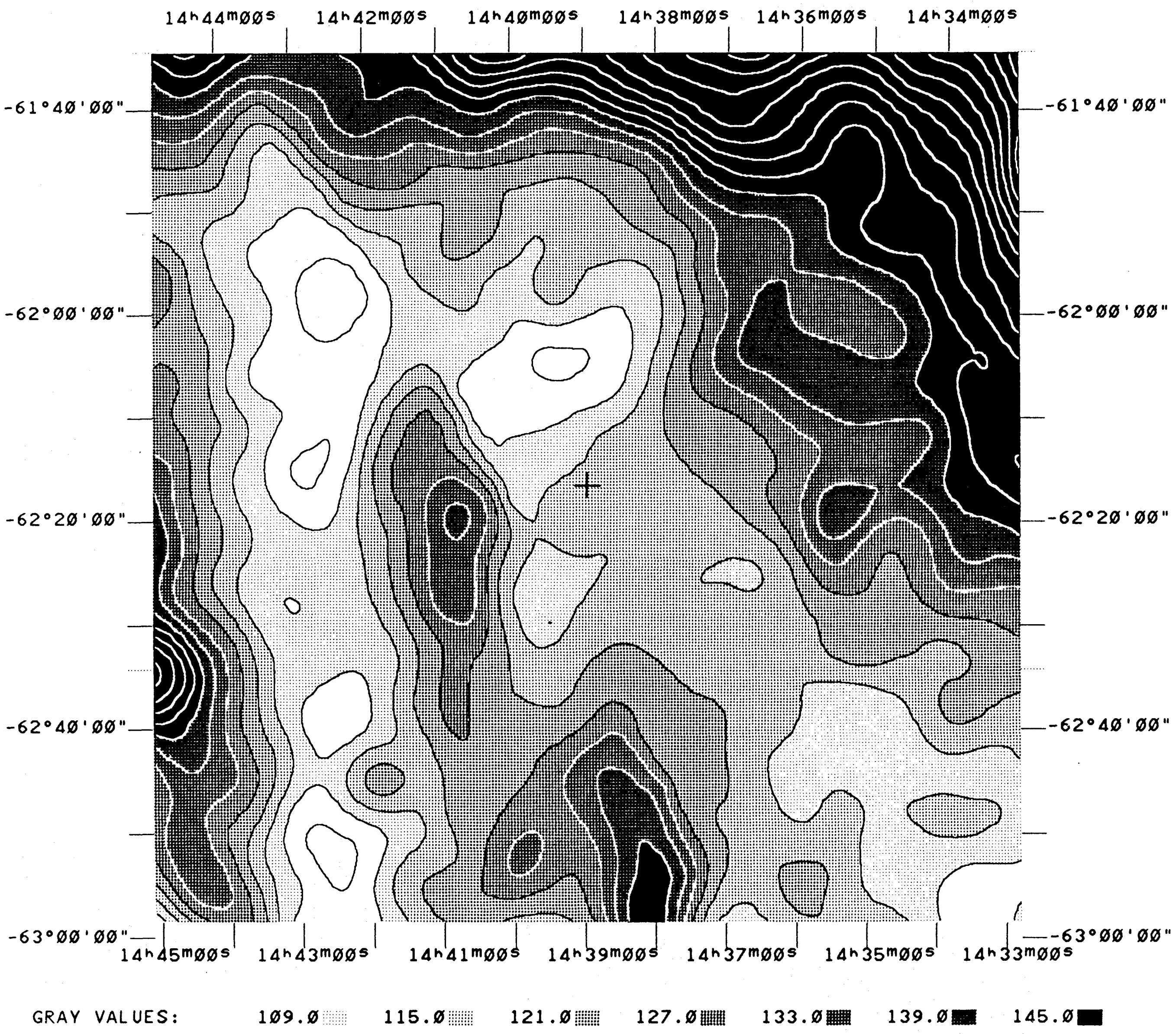

Fig. 4. Cold galactic dust component. The nominal center of RCW 86 is indicated. Grey scale and contours are linearly stepped by an increment of 6; units of MJy/sr in band 4

Table 2. Temperatures and column densities derived from the 60/100 ratio of the cold dust component, as a function of dust opacity model. DL 84 is the model of Draine & Lee (1984)

Opacity ($\propto \lambda^n$)	T_d (K)	N_H/I_{100} ($10^{18}\,\mathrm{cm}^{-2}/\mathrm{MJy\,sr}^{-1}$)
$n=0$	29.3	5.5
$n=-1$	25.1	12.3
DL 84	22.4	24.5
$n=-2$	22.0	28.7
Error	± 0.5	± 1.3

discussed by Draine & Lee (1984) at 100 μm. The Draine & Lee model ("DL 84") itself is very close to $n=-1.8$ at these wavelengths. For all these models, the expected fluxes in bands 1 and 2 would be zero. The cold dust spectrum may also be compared to those of Draine & Anderson (1985), who present calculations for an extended MRN (Mathis et al. 1977) grain size distribution with increased amounts of small (<0.01 μm) grains, the very small grains stochastically heated by the interstellar radiation field. However, none of their spectra fit either; for example the ones that have solar neighborhood interstellar radiation field strengths, combine an excess at 60 μm with a deficiency at 12 μm.

This indicates that also in Fig. 4 an overall hot component is present, which may not be surprising considering the direction of $l=315°$ and the large Skyflux beam. Nevertheless, the spectrum is constant, and Fig. 4 can be interpreted as a map of column densities by simply multiplying the brightness by the N_H/I_{100} ratio from Table 2. (The hot component will produce a minimal contribution to N_H.) Column densities towards RCW 86 vary between 2.5 and 3.7 10^{21} cm^{-2} using DL 84.

As may be seen in Fig. 1, there is a point source at $\alpha, \delta = 14^h37^m05^s, -62°32'52''$, unrelated to RCW 86, which blends in with the remnant's emission at the Skyflux resolution. This source also appears in the IRAS Point Source Catalogue and in the LRS data base, and is associated with CS 2178 from the General Catalogue of Cool Carbon Stars (Stephenson 1973); it can also be recognized in the optical on the ESO/SRC Southern Sky Atlas plates. An attempt was made to remove this source by a second spectral decomposition, this time of the Skyflux maps with the zodiacal component as determined above subtracted. For the cold dust and SNR components the same spectra were used as before, and CS 2178 was modeled as the third component. The result is summarized in Tables 3 and 4. The spectrum of CS 2178 can be fitted by a black body at $T = 1400 \pm 400$ K, or by a black body modified with an absorption efficiency $Q_{\rm abs}(\lambda) \propto \lambda^n$, giving e.g. $T = 285 \pm 40$ K for $n = -1$. The color correction factor is the ratio between in-band flux density and actual flux density at the nominal band center. The fluxes in Table 4 are not entirely mutually consistent (the flux ratios of Table 3 are), most notably in the difference between the survey co-add result and the others; this must be due to differences in the calibration of the various data sets. The spread for this particular object thus gives some indication of the uncertainties in the IRAS fluxes. In view of these discrepancies, and because the primary purpose of the co-add is to furnish a map while the Skyflux data is expected to give more accurate fluxes, the survey co-add values will not be used in the following.

This point source was also used to estimate the positional consistency between the IRAS products (PSC, survey co-add and three HCON's). A dispersion in positions of $1\sigma = 15''$ is found in both α and δ.

3. Results

3.1. Maps

The resulting maps of the infrared emission from RCW 86 are presented in Figs. 5 and 6. Figure 5 shows the SNR component, using the flux ratios for RCW 86 listed in Table 5 and the flux ratios for the zodiacal light, cold galactic dust and CS 2178 as given in the previous section. This map is indiscernable from band 3 with these latter 3 components subtracted. The brightest feature is the small arc centered at $\alpha, \delta = 14^h36\overset{m}{.}5, -62°28'$, which coincides with the southwestern rim of RCW 86. Also visible but very weak is an arc of emission at $\alpha, \delta = 14^h39^m, -61°58'$, coincident with the northern rim. The intensity reaches a maximum of 14 MJy/sr; the extended low level emission present in the map goes up to ~5 MJy/sr, and is mainly concentrated in a belt that runs from northeast to southwest; it is indicative of regions of higher temperature than the 22.4 K characterizing the bulk of the subtracted galactic dust (the brightness of which goes up to 45 MJy/sr in band 3). The correlation of this belt with the large scale distribution of the galactic dust (Fig. 4) indicates the level at which the assumption of a constant spectrum breaks down; changing the spectrum from the current values introduces other, small-scale and thus more disturbing correlations. This low level emission obscures the possible presence of the complete outline of RCW 86's shell. The map is an average of all three HCON's; there are only minor differences between the three, due to noise and residual striping.

Table 3. Flux ratios and color correction factors for CS 2178. PSC is the IRAS point source catalog

Band	PSC	Skyflux	Survey co-add	Color correction
1	1	1	1	1.3
2	0.29	0.31 ± 0.07	0.32 ± 0.03	1.45
3	< 0.14	0.04 ± 0.02	0.04 ± 0.02	1.5
4	< 1.6	0.00 ± 0.01	0.00 ± 0.01	~1.1

Table 4. Band 1 flux densities for CS 2178 from the various IRAS products

Data base	PSC	HCON-1	HCON-2	HCON-3	Survey co-add
Flux density (Jy)	47.4	44.7 ± 3	46.5 ± 3	39.1 ± 3	35.0 ± 0.3

A map of band 1 with zodiacal and galactic dust emission subtracted is empty except for stars, noise and residual striping (for all three HCON's). Band 2 with the zodiacal and galactic dust components subtracted is shown in Fig. 6. This image is also dominated by stars, including CS 2178 that falls on top of RCW 86's southwestern arc. The northern rim is more clearly seen than in band 3, but still at a barely significant level. At these levels, there are considerable variations between the three HCON's; for example the apparent brightening in the southwestern interior section of the remnant is only present in HCON-1. There are two other extended emission features in this map at comparable intensities. One is a relatively broad, sinuous vertical filament centered at $\alpha, \delta = 14^h41^m, -62°15'$; this is correlated with a dust filament (Fig. 4) and is probably a region where the galactic dust does not conform to the assumed spectrum, having an excess at 25 μm. Secondly, there is a curved filament trailing eastwards from the star at $\alpha, \delta = 14^h33\overset{m}{.}8, -61°15'$; this filament is also seen in the band 3 map, does not relate morphologically to RCW 86 and must be relatively hot fore- or background material.

Comparing these maps, and the survey co-add map (Fig. 1), with those published by Dwek (1988), there is agreement on the southwestern emission, but we cannot confirm the bright emission present in the center of Dwek's map. This may be due to a different interpretation of background features.

3.2. Fluxes

The flux densities of RCW 86 are listed in Tables 5–7 (in-band values); the errors contain contributions from background confusion (dominant) and the spread between the three HCON's. The data in Tables 5 and 6 apply to the 225 arcmin^2 region on the southwestern edge of RCW 86 where infrared emission is significantly detected, excluding all contamination from CS 2178. The northern rim (Table 7) may have a different spectrum, although the difference is not significant. The flux that may have been missed due to confusion within the 1385 arcmin^2 area of the remnant (using the radio and X-ray defined radius of 21′) is estimated to be less than 14 Jy at 60 μm.

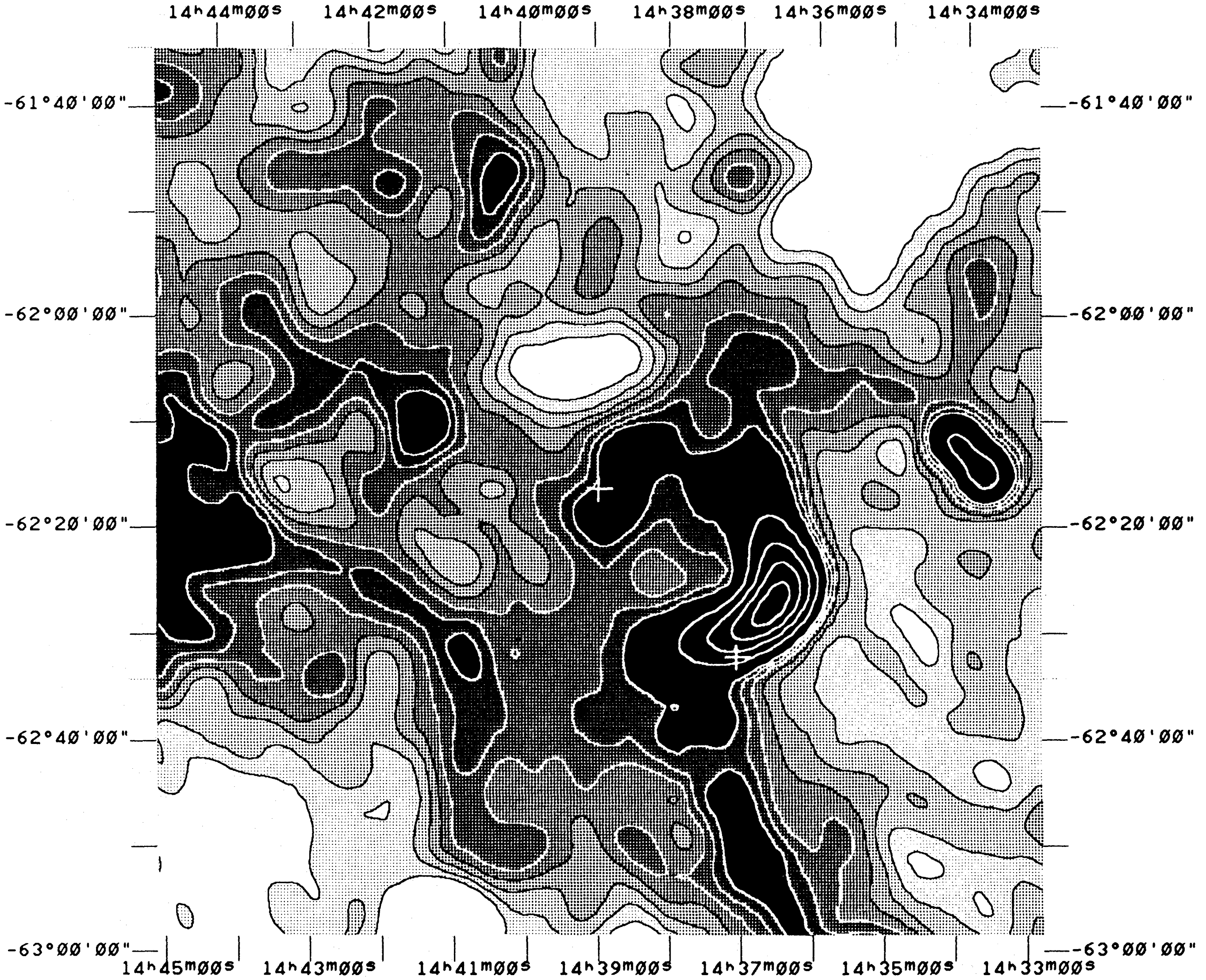

Fig. 5. Skyflux image of RCW 86 at 60 μm with zodiacal light, galactic dust and CS 2178 removed, which position like that of RCW 86's nominal center is indicated. The first 7 contours are linearly spaced by 0.4 and supported by a grey scale, the higher contours are spaced by 2 (MJy/sr in band 3)

Table 5. Flux ratios and color correction factors for the southwestern rim of RCW 86

Band	Flux ratio			Color correction
	Survey co-add	Skyflux	Adopted	
1	0.03±0.02	0.01±0.02	0.02±0.02	~1.8
2	0.30±0.05	0.24±0.04	0.26±0.04	0.83
3	1	1	1	1.03
4	0.37±0.4	0.74±0.2	0.67±0.2	1.05

Table 6. Infrared flux densities of the southwestern rim of RCW 86

Band	Flux (Jy)
1	0.0± 0.6
2	16 ± 2
3	66 ± 7
4	49 ±12

HCON	Band 3 flux (Jy)
1	71±6
2	65±6
3	63±6

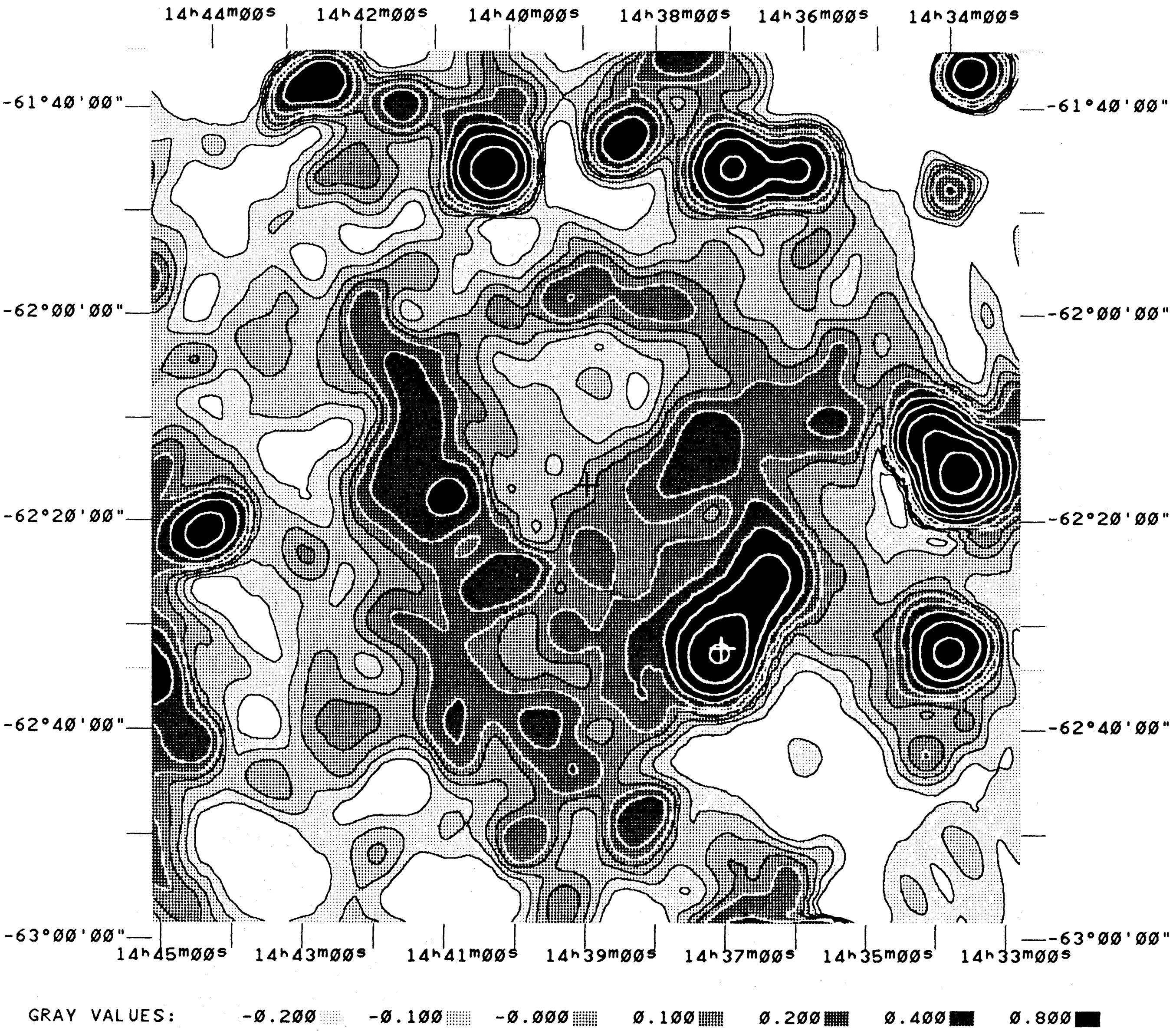

Fig. 6. Skyflux image of RCW 86 at 25 μm with zodiacal light and galactic dust removed. RCW 86's center and CS 2178 are indicated. The first 5 contours are linearly spaced by 0.1 (MJy/sr in band 2), the higher ones logarithmically by a factor of 2

Table 7. Results for the northern rim of RCW 86. The model is discussed in Sect. 4.2

Band	Flux ratio	Model	Flux density (Jy)	Color correction
1	0.20 ± 0.2	0.003	0.7 ± 0.7	1.22
2	0.45 ± 0.2	0.460	1.3 ± 0.4	0.85
3	1	1	3.6 ± 1.5	1.12
4	–	0.333	0 ± 11	1.11

3.3. Comparison with other wavelengths

The optical morphology of RCW 86 is described by a weak filament on the northern rim and a compact, almost hemispherically shaped set of brighter filaments in the southwest. The infrared maps were compared with plate number SR 134 of the ESO/SRC Southern Sky Atlas, fixing the position by SAO stars. At the Skyflux resolution, the southwestern infrared emission is coincident with the optical nebulosity there, but the survey co-add shows that the infrared maximum (at $\alpha, \delta = 14^h36^m44^s$, $-62°28'12''$) is $\sim 2'$ southeast of the optical centroid (at $\alpha, \delta = 14^h36^m33^s$, $-62°26'15''$); the infrared emission encompasses the optical. The northern optical filament coincides with the weak infrared northern rim, lending support to the reality of the infrared detection. (It should be remembered that the 1σ positional accuracy is $\sim 15''$.)

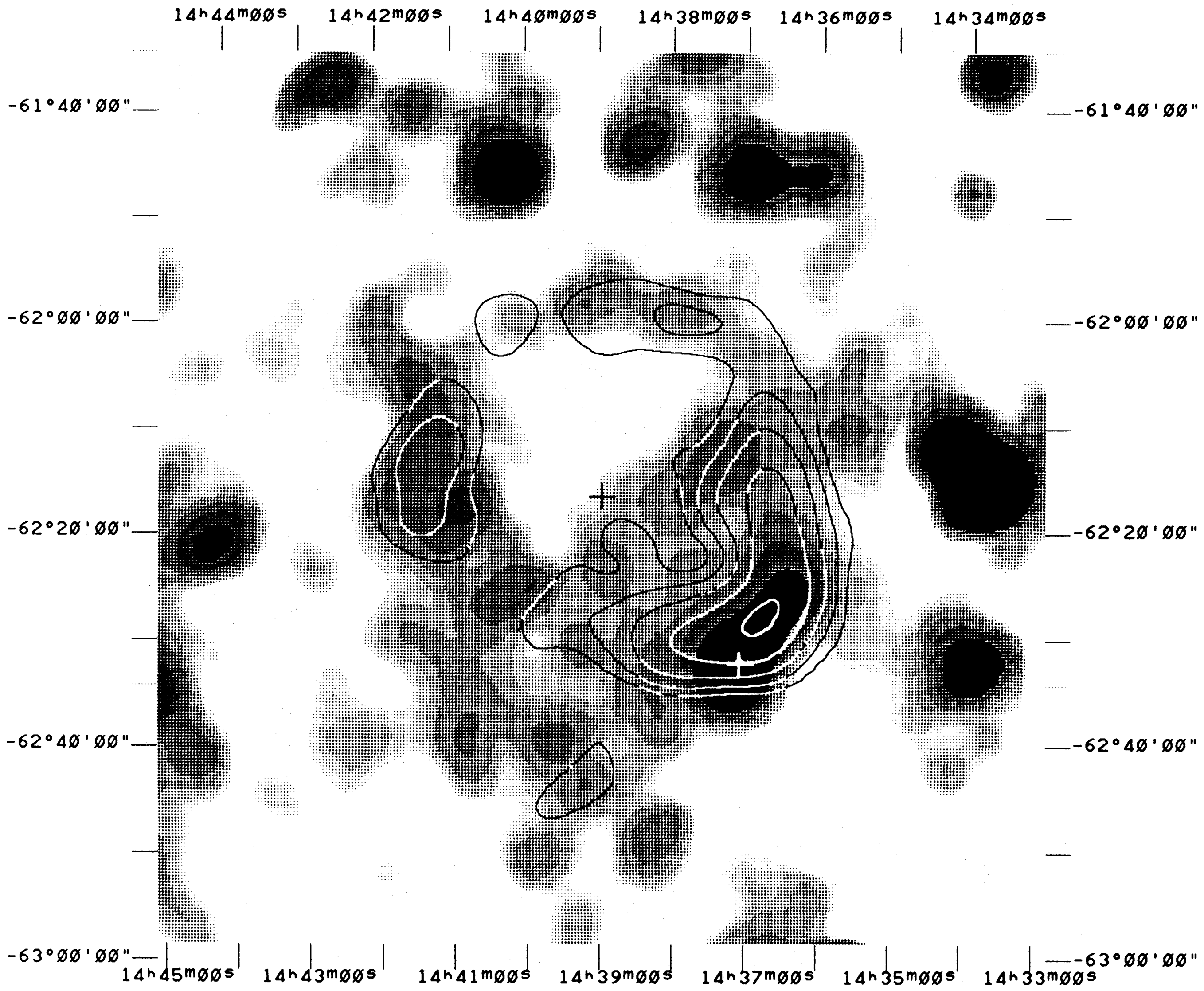

Fig. 7. RCW 86 at 25 μm (Fig. 6) in greys with EXOSAT LE contours overlaid. Both are logarithmically stepped. The LE image was kindly made available by J.J. Claas

The radio emission of RCW 86 as published in the 408 MHz (3′ resolution) map of Caswell et al. (1975) is characterized by an almost complete shell with a strong maximum in the southwestern corner and a relatively strong ridge along the eastern rim. The infrared maximum in the southwest is 2′ west of the radio maximum, i.e. in between the radio maximum and the optical centroid. The weak, extended infrared filament on the eastern side of RCW 86 that was discussed in the context of Fig. 6 does not follow the radio shell very well, confirming the idea that it is not associated.

X-ray images have been published by Pisarski et al. (1984) from the Einstein IPC (0.1–4 keV, 3′ resolution) and by Claas et al. (1989) from the Exosat LE experiment (0.05–2 keV, 1′ resolution). They show the same shell structure as in the radio, with the brightest part in the southwest, only the shell is more incomplete with additional emission mainly in the north and northeast. The correlation between the infrared and X-rays is very good, as can be seen in Fig. 7 which shows an overlay of the two, with the EXOSAT LE image smoothed to IRAS resolution; on the full resolution EXOSAT image, even the three weak 25 μm maxima on the northern rim have X-ray counterparts. The confusing broad eastern filament precludes a comparison in that area. The filament radially crossing the infrared shell on the west does not have an X-ray counterpart, but it bounds an X-ray inward protrusion on the north. Comparing the band 2 survey co-add map with the EXOSAT LE image, the southwestern infrared maximum is 35″ more outward than the X-ray maximum, a 2σ difference.

4. Interpretation

4.1. *Foreground material*

In Sect. 2.2 a total column density in the direction of RCW 86 which varies between $N_{\rm H} = 2.5$ and 3.7 (in units of 10^{21} cm^{-2}) was derived. This value may be compared with results from other authors. From optical spectra, Ruiz (1981) obtains $A_V = 0\overset{\rm m}{.}8$, corresponding to $N_{\rm H} = 0.6$ (using DL 84), while Leibowitz & Danziger (1983) find an average A_V of $1\overset{\rm m}{.}7$ corresponding to

$N_H = 1.3$. The total range in column density from the optical extinction found by these authors, which covers a factor of 10, is easily reconciled with the much smaller infrared range considering the different beam sizes and path lengths. Analysis of X-ray data gives for N_H 0.3 (Pisarski et al. 1984, assuming CIE), 1.1–4.4 (Nugent et al. 1984) and 1.3–3.3 (Claas et al. 1989); the two values quoted from the latter two authors correspond to the use of a CIE or NEI X-ray emission model respectively, hence the larger values may be more realistic. Although there is considerable spread in these estimates, most agree with the infrared determined N_H in the sense that they are lower, since in the direction $l, b = 315.^\circ4, -2.^\circ3$ only a fraction of the material along the line of sight is expected to be in front of RCW 86 (assuming a distance of ~ 1 kpc). The two N_H values needed for NEI fits are however rather high in this respect.

4.2. *Dust temperature and mass*

Extrapolating the radio spectrum measured between 408 and 5000 MHz, which is characterized by a spectral index of -0.62 (Caswell et al. 1975), the non-thermal contributions to the infrared emission are expected to be 0.08, 0.15, 0.25, 0.35 Jy for bands 1–4. The amount of atomic line emission present in the IRAS bands is more difficult to estimate. Dwek et al. (1987a) and Dinerstein et al. (1987) in an analysis of the young supernova remnant Cas A expect relatively small contributions, especially in the longer wavelength bands where the non-thermal is strongest. Considering the large errors in the IRAS fluxes of RCW 86, it can safely be assumed that essentially all of the infrared is thermal dust emission.

The infrared spectrum of RCW 86 (southwest) with its errors as quoted in Table 5 is consistent with a pure black body spectrum, or with a black body spectrum modified by an absorption efficiency of the form $Q_\lambda \propto \lambda^n$. For the unrealistic case of a pure black body ($n = 0$), the dust temperature derived is $T_d = 90 \pm 4$ K, while for $n = -1$, $T_d = 72 \pm 3$ K. Using the more realistic dust properties of the DL 84 [1] model, the dust temperature derived is $T_d = 65 \pm 3$ K. The mass of the dust M_d radiating at this temperature may be calculated using the expression for the flux density of the radiating dust

$$F_\nu = M_d B_\nu(T_d)\, \kappa_d(\nu)/D^2\,, \tag{1}$$

with B_ν the Planck function, D the distance, and where the effective mass absorption coefficient of the dust κ_d can be written as

$$\kappa_d(\nu) = (\varrho_C A_C \kappa_C + \varrho_{Si} A_{Si} \kappa_{Si})/(\varrho_C A_C + \varrho_{Si} A_{Si})\,, \tag{2}$$

considering that the dust is composed of graphite (C) and silicate (Si) particles (cf. Greidanus & Strom 1991). Here, ϱ_i is the density of a dust grain of species i while the grain size distribution is written as $dn_i(a) = n_H A_i a^{-3.5}\, da$ with n_H the gas density. Using $\varrho_C = 2.26\ \mathrm{g\,cm^{-3}}$, $\varrho_{Si} = 3.3\ \mathrm{g\,cm^{-3}}$, $A_C/A_{Si} = 0.891$, $\kappa_C = 145\ \mathrm{cm^2\,g^{-1}}$, $\kappa_{Si} = 95\ \mathrm{cm^2\,g^{-1}}$ (DL 84), a value of $\kappa_d = 115\ \mathrm{cm^2\,g^{-1}}$ at 60 µm is derived, which together with the color corrected 60 µm flux of 64.3 ± 6.8 Jy indicates $M_d = 5.8 \pm 0.6\ 10^{-4}\,M_\odot$ for the southwestern arc, at a distance of $D = 1$ kpc. The best-fitting dust temperature for the northern rim is $T_d = 75 \pm 10$ K, not significantly different from the southwest part. The "Model" column in Table 7 gives the spectrum for that temperature. The associated dust mass is $0.17 \pm 0.08\ 10^{-4}\,M_\odot$. The upper limit for the mass of dust radiating at $T_d = 65$ K that may be present within the outline of RCW 86 but which is not detected here is $1.2\ 10^{-4}\,M_\odot$.

The in-band flux ratios for dust at a temperature of 65 K with the DL 84 properties are 0.001, 0.243, 1, 0.412 (bands 1 through 4), which is 1.5σ from the measured values (southwest). It is possible to make a better fit with a two-temperature model. Assuming a hot and a cold component both constrained to the DL 84 model, and the cold component having the same temperature as the cold galactic dust ($T = 22.4$ K), the properties of these components that follow from the measured fluxes are given in Table 8 ($\kappa_d = 44\ \mathrm{cm^2\,g^{-1}}$ at $\lambda = 100$ µm). Changing the band 1 and 2 flux ratios of the cold component from 0.00 to 0.04 (as measured for the cold galactic dust) does not change any of the results significantly, nor does changing the band 3 flux ratio within ± 0.05.

At variance with the DL 84 model, other values for κ_d in the infrared have been published. For example, the extinction curve of Mezger et al. (1982) has $\kappa_d = 250\ \mathrm{cm^2\,g^{-1}}$ at 60 µm. This value would lower the dust mass associated with the hot component to $2.2 \pm 0.3\ 10^{-4}\,M_\odot$. Furthermore, it should be noted that although

Table 8. Results for a two-temperature model of the infrared emission of RCW 86 (southwestern part). The flux density is the color corrected value, at 60 µm for the hot component and at 100 µm for the cold component

Band	Hot component		Cold component	
	Flux ratio	Color corr.	Flux ratio	Color corr.
1	0.001	1.550	0.000	–
2	0.262	0.833	0.000	2.89
3	1	1.059	0.195	1.117
4	0.402	1.096	1	0.955
T_d (K)	66.5 ± 2.5		22.4	
Flux density (Jy)	$59\ \ \pm 7$		20 ± 14	
M_d ($10^{-3}\,M_\odot$)	0.48 ± 0.07		30 ± 20	

---

[1] Draine & Lee (1984), tabulated in Drain (1985), give absorption efficiencies for silicate and graphite dust particles as a function of grain radius (a) and wavelength, and follow the MRN size distribution (Mathis et al. 1977) between $a_{\min} = 0.005$ µm and $a_{\max} = 0.25$ µm, keeping the total gas to dust mass ratio at 100.

M_d in Eq. 1 appears to be of the form nV, it is actually of the form $\int n^2\, dV/\bar{n}$ if the dust is collisionally heated.

4.3. *Comparison with X-ray results*

Dwek (1987) has made calculations of the infrared luminosity function of a dusty plasma. In this model, dust grains immersed in a hot gas are heated by collisions with thermal electrons and ions, and radiate thermally in the infrared. The essential features of the model are that the luminosity L_{gr} of a dust grain, and hence through its optical properties its temperature T_d, are determined by the collisional heating H of the grain, assuming an equilibrium situation:

$$L_{gr}(a, T_d) = nH(a, T)\,, \tag{3}$$

with a the grain radius and n and T the plasma density and temperature. With the infrared luminosity defined as

$$L_{\rm IR} = R\Lambda_{\rm IR}(T_{\rm X}) \int n_e n_{\rm H}\, dV\,, \tag{4}$$

where R is the dust to gass mass ratio, n_e and $n_{\rm H}$ are the electron and hydrogen density and V is the volume of the hot plasma, the infrared luminosity function $\Lambda_{\rm IR}$ is then a function of the gas temperature $T_{\rm X}$ and of the optical properties of the dust grains only; it is independent of the gas density. Because the X-ray luminosity can be written in the same form as Eq. 4 (dropping R), the ratio of infrared to X-ray luminosity is also a function of gas temperature and R only. This ratio is a large number, >10 for $T_{\rm X} > 0.3\ 10^7$ K ($R = 0.01$), indicating that infrared cooling dominates over X-ray cooling.

In the context of this model, the infrared flux density can be related to the X-ray flux density most usefully with the help of the (distance independent) emission normalization constant:

$$C_{\rm IR} = \int n_e n_{\rm H} dV/D^2 = 4\pi F_{\rm IR}/R\Lambda_{\rm IR}(T_{\rm X})\,, \tag{5}$$

and $C_{\rm X}$ analogously defined. Taking the gas temperature $T_{\rm X}$ from X-ray measurements, $C_{\rm IR}$ and $C_{\rm X}$ should be equal, since the X-rays and infrared radiation are expected to come from the same elements of gas. Estimating the 60 µm flux density of the whole remnant, including emission below the sensitivity, to be 75 ± 10 Jy, and using the derived dust temperature of $T_d = 65$ K, $F_{\rm IR} = 6.5 \pm 0.9\ 10^{-9}$ erg s^{-1} cm^{-2} by

$$\frac{F_{\rm IR}}{F_\nu} = \frac{\sigma T_d^4\, \bar{\kappa}_d(T_d)}{\pi B_\nu(T_d)\, \kappa_d(\nu)}\,, \tag{6}$$

where $\bar{\kappa}_d(T_d)$ is defined analogously to $\kappa_d(\nu)$ [Eq. (2)] in terms of $\kappa_{\rm C}$ and $\kappa_{\rm Si}$, with $\bar{\kappa}_i = (3/4)\,\varrho_i^{-1}\,\bar{Q}_i/a$, $\bar{Q}_i$ the Planck-averaged absorption efficiency of a grain of species i; $\bar{\kappa}_d = 144$ cm^2 g^{-1} at $T_d = 65$ K, (almost) independent of a (DL 84).

The most recent X-ray observations of RCW 86 are summarized in Table 9. Pisarski et al. (1984) (entry 3 in the table) fitted a one component CIE model to Einstein IPC data (0.1–4 keV). Nugent et al. (1984) analyzed HEAO 1 A-2 spectra (0.5–15 keV), and found for CIE a low (entry 1) and a high temperature (entry 5) component; for NEI, one temperature suffices (entry 5^N). Claas et al. (1989) fitted EXOSAT spectra (0.2–10 keV) and found a low temperature CIE component (entry 2) and also fitted NEI (entry 4), Where necessary, quoted $C_{\rm X}$ values have been brought to the present definition [Eq. (5)] using $n_e/n_{\rm H} = 1.2$. The values for $C_{\rm IR}$ corresponding to these temperatures, assuming $R = 0.01$, are added in the table, as are the values for R assuming $C_{\rm IR} = C_{\rm X}$. There is a large spread in these values of R, related to the interpretation of the X-ray temperatures. If the CIE model is correct, the low temperature flux can be ascribed to the reverse shocked ejecta and the high temperature one to the SN blast wave through the interstellar medium. The R^{-1} values in the table are calculated assuming that all infrared emission arises either in the ejecta (entries 1 and 2, implying the absence of dust from the surrounding medium) or in the interstellar medium (entries 4 and 5, implying the absence of dust from the ejecta); the resulting numbers are thus lower limits on R^{-1}, hence $R_{ej}^{-1} \gtrsim 500$ and $R_{ism}^{-1} > 500$. When $R_{ej} = R_{ism}$ is assumed, $R^{-1} \approx 1200$. Alternatively, attributing the low temperature component to NEI effects, the resulting value of $R^{-1} \approx 850$ (entries 4 and 5^N). Thus, either interpretation indicates a shortage of dust with respect to standard values. The quoted errors for the $C_{\rm X}$ are generally $\sim 5\%$, the error in $C_{\rm IR}$ is $\sim 15\%$ from $F_{\rm IR}$, and Dwek et al. (1987b) estimate $\Lambda_{\rm IR}$ to be accurate to better than $\sim 40\%$.

This outcome may be compared with the analysis of RCW 86 by Dwek et al. (1987b), who arrive at the opposite result and find an infrared excess using the same infrared emission model. The difference can be attributed to the following effects. Firstly, the infrared flux they obtain for RCW 86 is a factor of ~ 3 over the present result; this is most likely caused by the different methods used for the background subtraction in combination with the heavy confusion (cf. the discrepancy between the maps, Sect. 3.1). The currently derived infrared flux density would put RCW 86 closer to the predicted curve in Dwek et al.'s Fig. 1, indicating more normal values for the dust to gas ratio. Secondly, however, they use the X-ray flux density of Pisarski et al. (1984) and correct that for NEI effects by dividing it by a factor 9, obtained from the models of Hamilton et al. (1983). Following the same procedure, we derive $R^{-1} = 51$ (entry 3^N in Table 9). The discrepancy of this number with respect to all other values purely reflects a discrepancy in the X-ray results. As Pisarski et al. base their spectral analysis on IPC data, while Nugent et al. and Claas et al. use dedicated instruments, we believe the latter results to be more reliable.

Table 9. Comparison of X-ray and infrared results (see text)

Ref.	$T_{\rm X}$ (10^7 K)	$C_{\rm X}$ (10^{13} cm^{-5})	$C_{\rm IR}$ (R/0.01) (10^{13} cm^{-5})	R^{-1}	$n_{0,\rm IR}$ (cm^{-3})
1	0.6	8.5	4.4	200	2.3 ± 0.4
2	0.6	38.7	4.4	880	2.3 ± 0.4
3	1.4	11.1; 1.2^N	2.4	460; 51	1.0 ± 0.2
4	3.9	11.4^N	1.6	710	0.6 ± 0.1
5	5.9; 6.3^N	7.4; 15^N	1.4	520; 1020	0.6 ± 0.1

N: using NEI

It is not likely that the apparent depletion of the dust in RCW 86 is caused by sputtering, which destroys the shocked dust, since sputtering timescales are of the order of $t \sim 10^5/n \gg 1800$ yr, with $n \sim 4\,\mathrm{cm}^{-3}$ (Draine 1981). Alternatively, the dust may not be coupled to the plasma. This occurs if the Larmor radius r_L of the dust particles is large with respect to the shock zone. For a magnetic field of $B = 1\,\mu$G, $r_L \sim 0.03$ pc, scaling with B^{-1} (Dwek 1987). The effective thickness of a Sedov shock is $r_s/12 = 0.5$ pc for RCW 86 at 1 kpc, hence $B < 0.1\,\mu$G is needed to uncouple the dust from the hot gas. Alternatively, if the emission is from shocked clouds (instead of from a blast wave through a homogeneous medium), a compressed region of 0.03 pc is built up in only 17 yr with a shock speed of $1700\,\mathrm{km\,s}^{-1}$ (corresponding to $4\;10^7$ K), so also in that case a low B is needed. Such low B values are very improbable, however, considering typical interstellar magnetic field strengths of $\sim 3\,\mu$G and up to $\sim 20\,\mu$G within H I clouds (Vallée 1983). Moreover, from the radio flux density and spectral index (Caswell et al. 1975) the magnetic field strength may be estimated based on a minimum (equipartition) energy argument (Pacholczyk 1970), giving $B \sim 80\,\mu$G, a number which is rather insensitive to its input parameters (notably $\propto D^{-2/7}$). If we want to retain the notion that the infrared deficiency is caused by a low magnetic field strength, however, the conclusion is that this must be local to the hot X-ray emitting gas and that the magnetic field is concentrated in the radio emitting regions. This picture is in any case consistent with the lack of small-scale correlations between the radio and X-ray morphology generally seen in supernova remnants, cf. for RCW 86 the HRI image (Pisarski et al. 1984) and the MOST map (Kesteven & Caswell 1987).

Other possibilities to explain the infrared/X-ray discrepancy include a misinterpretation of the X-ray spectra and a misunderstanding of the physics involved in the electron- and ion-grain collisions that form the basis of the infrared emission model. In their infrared/X-ray comparison of eight other supernova remnants, Dwek et al. (1987b) find five remnants to be significantly deficient in infrared emission, and three to be consistent with the model, making the above considerations applicable to more remnants than RCW 86 alone.

4.4. Density

Although the total infrared luminosity of the dust grains does not depend on the gas density, their temperature does (Dwek 1987). Using this effect, gas densities ($n_{0,\mathrm{IR}}$) that follow from $T_d = 65$ and T_X are listed in Table 9 as well, after conversion to pre-shock values ($n_0 = n_\mathrm{H}/4$). These densities are independent of the gas to dust ratio. For the interstellar medium surrounding RCW 86, a pre-shock density of $0.6 \pm 0.1\,\mathrm{cm}^{-3}$ is indicated (table entries 4 and 5). For possible ejecta, $n_{0,\mathrm{IR}} = 2.3 \pm 0.4\,\mathrm{cm}^{-3}$. When the effective volume of the emitting gas is calculated using a projected shell radius of 20′, a relative shell thickness of 1/12 and a distance of 1 kpc, the C_X values of the various authors imply pre-shock densities between 0.08 and $0.2\,\mathrm{cm}^{-3}$, with the NEI values at 0.11. These values are significantly smaller than the infrared one; however, this volume must overestimate the actual effective volume associated with the X-ray emission, as can be established from the X-ray maps, and by the same token, the infrared-derived density comes mainly from the emission of the southwestern arc. Claas et al. (1989) treat the southwest region separately in their analysis and derive for the density a value of $1.1 \pm 0.3\,\mathrm{cm}^{-3}$, as opposed to 0.11 for the remainder of the remnant, in better agreement with the infrared value. In spite of this density difference, Claas et al. find a lack of spectral variation over the remnant, indicating that all regions are approximately at the same temperature. This is in accordance with the good infrared/X-ray correlation, since $\Lambda_\mathrm{IR}/\Lambda_\mathrm{X}$ varies by a factor of ~ 10 between $T_\mathrm{X} = 0.5$ and $5\;10^7$ K.

5. Comparison with other young remnants

We can compare our results on RCW 86 with what is known about the infrared emission from other young supernova remnants, in particular the shell remnants Tycho, Kepler and Cas A. Braun (1987) presents and discusses the results of IRAS observations of these objects, and we have mapped the brightest part of Cas A at $20\,\mu$m using UKIRT (Greidanus & Strom 1991). In the infrared, Tycho and Cas A display the most complete shells, while in both Kepler and RCW 86 the emission is dominated by a relatively small region. The dominant region is also that with the brightest optical nebulosity, and this underlines an apparent correlation between the optical and infrared emission, which can be traced to a very significant extent in Tycho and is also evident in Cas A (Braun 1987), though it is not apparent on the scale of individual knots in the latter (Greidanus & Strom 1991).

Salient infrared parameters for the four shells are summarized in Table 10 and compared to X-ray derived parameters. The infrared parameters for Tycho, Kepler and Cas A were derived

Table 10. Infrared and X-ray parameters of four historical shell-type supernova remnants

		RCW 86	Tycho	Kepler	Cas A
Age	(yr)	1800	417	385	300
D	(kpc)	1	2.3	4.1	2.9
T_d	(K)	65 ± 3	80.5 ± 1.5	95 ± 1	103.5 ± 1.5
L_IR	($10^3\,L_\odot$)	0.20 ± 0.03	0.8 ± 0.1	0.9 ± 0.1	6.3 ± 0.9
M_d	($10^{-3}\,M_\odot$)	0.6 ± 0.1	0.8 ± 0.1	0.37 ± 0.06	1.8 ± 0.3
$n_{0,\mathrm{IR}}$	(cm^{-3})	0.6 ± 0.1	1.6 ± 0.1	3.2 ± 0.2	5.0 ± 0.3
T_X	(10^7 K)	3.9 ± 0.2	7.6 ± 0.6	6.1 ± 2	4.34 ± 0.06
$M_{\mathrm{sw,X}}$	($M_\odot$)	4.9 ± 0.5	3.3 ± 0.04	1.8 ± 0.5	5.8 ± 1.2
$n_{0,\mathrm{X}}$	(cm^{-3})	1.1 ± 0.3 [a]	1.1 ± 0.1	1.3 ± 0.4	5.7 ± 1.2

[a] Southwestern part

from the flux densities listed by Braun (1987), in the same way as they have been calculated for RCW 86; the total infrared luminosity L_{IR} is based on Eq. 6. The X-ray parameters T_{X}, $n_{0,\mathrm{X}}$ and $M_{\mathrm{sw,X}}$ (the swept-up mass) are taken from Claas et al. (1989) for RCW 86, from Smith et al. (1988) for Tycho, from Smith (1988) for Kepler and from Jansen et al. (1988) for Cas A. Phenomenologically, there is a trend for the remnants to get cooler and less luminous in the infrared with age, while the X-ray temperatures vary more randomly. In the context of the collisionally heated dust model, this result must be at least partly spurious: assuming a Sedov evolution, the dust temperature is only a very weak function of age, primarily dependent upon density, while the total infrared luminosity is in fact expected to increase with age (as long as sputtering is unimportant).

This trend is indeed not followed by the fifth historical shell-type supernova remnant, SN 1006. From a spectral decomposition of the Skyflux HCON-1 maps, 1-σ upper limits for the flux density in IRAS bands 1–4 of about 3, 3, 6, and 3 Jy are estimated for this object. At a distance of 1.5 kpc, this implies upper limits on the total infrared luminosity of 0.04–0.08 $10^3\,L_\odot$ and on the dust mass of 0.1–0.02 $10^{-3}\,M_\odot$, assuming that the temperature is within the range of 65–103 K spanned by the other four remnants. These low values are probably a result of its relatively high elevation above the galactic plane, which would place SN 1006 in a low density region.

The second conclusion that can be drawn from this table is that the independently derived infrared and X-ray pre-shock densities (n_0) are in all cases comparable, strengthening the credibility of the models used, at least as far as the temperatures are concerned. The largest deviations, by a factor of ~ 2, occur for RCW 86 and Kepler; this is possibly related to these remnants being the weakest and most inhomogeneous ones. It can be noted here that although the literature values for the X-ray temperatures show a large spread (cf. Table 9), a factor of 2 change in T_{X} changes $n_{0,\mathrm{IR}}$ only by $\sim 30\%$.

In the third place, the X-ray masses are an order of magnitude larger than the infrared masses: the ratio $M_{\mathrm{sw,X}}/100\,M_d$ ranges from 30 in Cas A to 80 in RCW 86. This implies that even for a large gas to dust ratio like 500–1000, as was suggested for RCW 86 in Sect. 4.3, the X-ray masses must be significantly overestimated, or, alternatively, the infrared luminosity is much smaller than expected.

Finally, Cas A with its higher luminosity, mass, and density stands somewhat apart from the others. This may reflect a location in a denser environment, possibly due to pre-SN mass loss, or alternatively it may signalt the presence of dust in the ejecta. Whereas the other three remnants are thought to result from Type I supernovae, Cas A is also the only one with (probably) a massive progenitor.

6. Conclusions

Through the use of a destriping and a spectral decomposition technique, we have been able to isolate the weak infrared emission of RCW 86 from all other contributions in the IRAS maps, which are zodiacal light (at black body temperatures between 245 and 380 K), cold galactic dust (at 22.4 K assuming DL 84 emissivities) and the cool carbon star CS 2178 ($T \approx 1400$ K). The infrared maps correlate very well with the X-ray brightness distribution, in accordance with the Dwek (1987) model for the infrared emission considering the isothermal nature of the X-ray distribution. With a 1σ positional accuracy of 15″, there is no significant radial displacement with respect to the X-ray emission. A total infrared flux density for RCW 86 of $6.5 \pm 0.9\ 10^{-9}$ erg s^{-1} cm^{-2} is derived, with a maximum at 60 µm of 75 ± 10 Jy, mainly from the southwestern part of the remnant. The infrared is most probably thermal emission from shock-heated dust, and the derived dust temperature is 65 ± 3 K. The mass of hot dust is $0.6 \pm 0.1\ 10^{-3}\,M_\odot$. A pre-shock density of 0.6 ± 0.1 cm^{-3} is derived for the surrounding medium, in reasonable agreement with X-ray results for the southwestern part. If the low temperature X-ray component arises in the reverse-shocked ejecta, a pre-shock density of 2.3 ± 0.4 cm^{-3} is implied for these. With respect to the emission model of Dwek (1987) and standard dust to gas mass ratios, the infrared flux is deficient by a factor of ~ 10, although the large discrepancies between the various X-ray results and interpretations in the literature complicate the analysis. Considering the young age of the remnant, this deficiency cannot be caused by grain destruction. Possible explanations are: (1) the dust to gas mass ratio is $\sim 1/850$; (2) the dust is not well-coupled to the gas, implying that the magnetic field is concentrated in the radio emitting regions and rarefied throughout most of the X-ray emitting gas; (3) the X-ray and/or infrared emission models are systematically in error, respectively over- or underestimating the emissivity.

When RCW 86 is compared with the three other young shell-type remnants Tycho, Kepler and Cas A, it is found that the dust temperatures and luminosities decrease with age, a result, however, which is spurious in the context of the infrared emission model. For all objects, the infrared and X-ray based densities are similar, while the X-ray derived masses are an order of magnitude above the infrared ones. Cas A is hotter and brighter in the infrared than the other three, clearly related to its more massive progenitor.

Acknowledgements. We are indebted to the IRAS team for furnishing the observations, and to R. Braun, P. Schwering, E. Deul and R. Walterbos for providing valuable ideas and software. The Netherlands Foundation for Research in Astronomy is financially supported by the Netherlands Organization for Scientific Research (NWO).

References

Beichmann, C.A., Neugebauer, G., Habing, H.J., Clegg, P.E., Chester, T.J. (eds.), 1988, IRAS Catalogs and Atlases 1 (Explanatory Supplement), NASA, Washington, D.C.
Berkhuijsen, E.M., 1986, A & A 166, 257
Braun, R., 1985, P.D. Thesis, Leiden University
Braun, R., Strom, R.G., van der Laan, H., Greidanus, H., 1986, in Light on Dark Matter, ed. F.P. Israel, Reidel, Dordrecht, p. 47
Braun, R., 1987, A & A 171, 233
Caswell, J.L., Clark, D.H., Crawford, D.F., 1975, Aust. J. Phys. Astrophys. Suppl. 37, 39
Claas, J.J., Smith, A., Kaastra, J.S., de Korte, P.A.J., Peacock, A., 1989, ApJ 337, 399
Clark, D.H., Caswell, J.L., 1976, MNRAS 174, 267
Clark, D.H., Stephenson, F.R., 1977, Historical Supernovae, Pergamon, Oxford
Dennefeld, M., 1986, A & A 157, 267
Deul, E.R., Wolstencroft, R.D., 1988, A & A 196, 277
Dinerstein, H.L., Lester, D.F., Rank, D.M., Werner, M.W., Wooden, D.H., 1987, ApJ 312, 314
Draine, B.T., 1981, ApJ 245, 880

Draine, B.T., Lee, H.M., 1984, ApJ 285, 89 (DL 84)
Draine, B.T., 1985, ApJS 57, 587
Draine, B.T., Anderson, N., 1985, ApJ 292, 494
Dwek, E., Dinerstein, H.L., Gillet, F.C., Hauser, M.G., Rice, W.L., 1987a, ApJ 315, 571
Dwek, E., Petre, R., Szymkowiak, A., Rice, W.L., 1987b, ApJ 320, L27
Dwek, E., 1987, ApJ 322, 812
Dwek, E., 1988, in Supernova Remnants and the Interstellar Medium, eds. R.S. Roger, T.L. Landecker, Cambridge Univ. Press, Cambridge, p. 363
Green, D.A., 1984, MNRAS 209, 499
Greidanus, H., Strom, R.G., 1991, 20 micron observations of Cassiopeia A, A&A (submitted)
Hamilton, A.J.S., Sarazin, C.L., Chevalier, R.A., 1983, ApJS 51, 115
Huang, Y.-L., Thaddeus, P., 1985, ApJ 295, L13
Huang, Y.-L., Moriarty-Schieven, G.H., 1987, Sci. 235, 59
Ilovaisky, S.A., Lequeux, J., 1972, A&A 18, 169
Jansen, F.A., Smith, A., Bleeker, J.A.M., de Korte, P.A.J., Peacock, A., White, N.E., 1988, ApJ 331, 949
Kesteven, M.J., Caswell, J.L., 1987, A&A 183, 118
Leibowitz, E.M., Danziger, I.J., 1983, MNRAS 204, 273
Lucke, R.L., Zarnecke, J.C., Woodgate, B.E., Culhane, J.L., Sooker, D.G., 1979, ApJ 228, 763
Mathis, J.S., Rumpl, W., Nordsieck, K.H., 1977, ApJ 217, 425
Mezger, P.G., Mathis, J.S., Panagia, N., 1982, A&A 105, 372
Milne, D.K., 1970, Aust. J. Phys. 23, 425
Naranan, S., Shulman, S., Yentis, D., Fritz, G., Friedman, H., 1977, ApJ 213, L53
Neugebauer, G., Habing, H.J., et al., 1984, ApJ 278, L1
Nugent, J.J., Pravdo, S.H., Garmire, G.P., Becker, R.H., Tuohy, I.R., Winkler, P.F., 1984, ApJ 284, 612
Pacholczyk, A.G., 1970, Radio Astrophysics, Ch. 7.3, Freeman, San Francisco
Pisarski, R.L., Helfland, D.J., Kahn, S.M., 1984, ApJ 277, 710
Ruiz, M.T., 1981, ApJ 243, 814
Smith, A., 1988, in Supernova Remnants and the Interstellar Medium, eds. R.S. Roger, T.L. Landecker, Cambridge Univ. Press, Cambridge, p. 119
Smith, A., Davelaar, J., Peacock, A., Taylor, B.G., Morini, M., Robba, N.R., 1988, ApJ 325, 288
Stephenson, C.B., 1973, Publ. Warner & Swasey Obs. 1, No. 4
Vallée, J.P., 1983, J. Roy. Astron. Soc. Canada 77, 177
Westerlund, B.E., 1969, AJ 74, 879
Winkler, P.F., 1978, ApJ 221, 220